# A Novel Perovskite $SrTiO_3$-$Ba_2FeNbO_6$ Solid Solution for Visible Light Photocatalytic Hydrogen Production

*Guoqiang Zhang, Shaorui Sun, Wenshuai Jiang, Xiang Miao, Zhao Zhao, Xiaoyan Zhang, Dan Qu, Duoying Zhang, Dabing Li, and Zaicheng Sun**

The photocatalytic splitting of water into molecular hydrogen and oxygen or reducing $CO_2$ using sunlight represents a promising solution to the looming energy crisis.[1] According to the reports,[2] oxides such as transition metal oxides and perovskite type oxides are ideal photocatalysts for water splitting. However, the fatal challenge is wide band gap of these oxides due to their fundamental characteristics of the metal–oxygen. The excitation across the band gap is essentially a charge transfer from the oxygen (O) 2*p* states at the valence band maximum to the transition-metal *d* states at the conduction band minimum. Owing to a large difference in electronegativity between the oxygen and transition-metal atoms, the band gap is quite large (3–5 eV). The development of visible-light photocatalysts, therefore, has become one of the most important topics in photocatalytic research today. Traditional visible-light photocatalysts are either unstable (CdS, CdSe, etc.)[3] or low activity ($Fe_2O_3$, $WO_3$, etc.).[4] Recently, some UV-active oxides are turned into visible-light photocatalysts by substitutional doping of metals as in $Ni_xIn_{1-x}TaO_4$[5] and (V-, Fe-, or Mn-) $TiO_2$,[6] or C, N, and S, as in $TiO_{2-x}N_x$,[7] $TiO_{2-x}C_x$,[8] and a series of oxynitrides such as TaON, $BaTaO_2N$, $SrNbO_2N$, $LaTiO_2N$, and $LaMg_xTa_{1-x}O_{1+3x}N_{2-3x}$ exhibit photoelectrochemical water splitting.[9] However, these oxynitrides are mostly unstable upon light irradiation; appropriate surface modifications are required to suppress the competitive oxidation of $N^{3-}$ by photogenerated holes.[9e,10] It is highly desired to develop oxides for stable visible light photocatalysts.

Perovskite oxides ($ABO_3$) are one of the most important families of materials exhibiting suitable properties for numerous technological applications.[11] For example, $SrTiO_3$ and others have shown excellent photocatalytic properties in UV region.[12] The A site is occupied by the larger cation, while the B site is occupied by the smaller cation in $ABO_3$ crystal structure. Generally, cations at B site are strongly bonded with the oxygen, while A site cations have relatively weaker interactions with oxygen. Perovskites may exhibit different electronic and optical properties depending on the ionic radius and electronegativity of the B site cations.[13] According to the energy band engineering strategy explored in a previous theoretical study,[14] it has been demonstrated that $BO_6$ tilting distortions from the ideal high-symmetry cubic $ABO_3$ structure have a strong impact on the band gap of perovskites. Recently, Rappe and co-workers have confirmed that perovskites with narrow band gap are constructed by using two different transition-metal cations on the perovskite B site, which resulting in B-cation off-center displacement due to different ionic radius.[15] They mixed the perovskite ferroelectric oxide $KNbO_3$ with $BaNi_{1/2}Nb_{1/2}O_{3-\delta}$ to introduce Ni to the B site and oxygen vacancies, which give band gap in the resulting $[KNbO_3]_{1-x}[BaNi_{1/2}Nb_{1/2}O_{3-\delta}]_x$ materials of 1.1–2.0 eV matching the solar spectrum well. Rosei and co-workers have demonstrated an effective approach to tune the band gap of double perovskite multiferroic oxides by engineering the cationic order for the case of $Bi_2FeCrO_6$.[16] A power conversion efficiency of 8.1% under AM 1.5G irradiation (100 mW $cm^{-2}$) for $Bi_2FeCrO_6$ thin-film solar cells in a multilayer configuration is successfully constructed. Chen and co-workers also demonstrated that ferroelectric materials can be served as photovoltaic materials due to a potentially large build-in electrical field and narrow band gap.[17] This strategy could be extended to the photocatalysis field to develop oxide-base visible light photocatalysts. However, the investigation on the photocatalytic properties of this type of oxides still remains to explore.

Herein, we synthesize a new type of perovskite $Ba_2FeNbO_6$ (BFNO) with mixed $Fe^{3+}$ and $Nb^{5+}$ on the B site, which exhibits a strong visible light absorption up to 550 nm ($E_g$ = 2.29 eV). It indicates that perovskite oxides with narrow band gap can be obtained via substituting metal elements on the B site. This further confirms that the elements on the site B have a strong effect on the band gap, thus, we can utilize this strategy to narrow the band gap of perovskites. However, it still exhibits low photocatalytic performance due to poor charge separation efficiency. In order to promote the photocatalytic performance, the solid solutions of $SrTiO_3$-$Ba_2FeNbO_6$ (STO-BFNO) nanocrystals are prepared via molten salts route. X-ray diffractometer (XRD) and electron energy loss spectroscopy (EELS) mapping images indicate the STO-BFNO solid solutions are uniformly formed.

G. Zhang, X. Miao, Z. Zhao, X. Zhang, D. Qu, Prof. D. Li
State Key Laboratory of Luminescence and Applications
Changchun Institute of Optics
Fine Mechanics and Physics
Changchun, 130033 Jilin, P. R. China
G. Zhang, X. Miao, Z. Zhao, X. Zhang, D. Qu
University of Chinese Academy of Sciences
Beijing 100000, P. R. China
Prof. S. Sun, W. Jiang, Prof. Z. Sun
Beijing Key Laboratory of Green Catalysis and Separation
Department of Chemistry and Chemical Engineering
School of Environmental and Energy
Beijing University of Technology
100 Pingleyuan, Changyang District, Beijing 100124, P. R. China
E-mail: sunzc@bjut.edu.cn
Prof. D. Zhang
Department of Electronic Engineering
Jinan University
Guangzhou 510632, P. R. China

DOI: 10.1002/aenm.201600932

  

The band gap ($E_g$) of solid solutions can be gradually tuned from 3.31 eV for $SrTiO_3$ to 2.29 eV for BFNO by changing the molar ratio of STO/BFNO. The solid solutions exhibit good visible light photocatalytic performance and stability. The highest photocatalytic $H_2$ production rate is 7.15 μmol $h^{-1}$ for 50 mg photocatalyst under irradiation of visible light ($\lambda > 420$ nm).

As Grinberg et al. demonstrate that the band gap can be narrowed by using mixed elements at B site in the $ABO_3$ type perovskite to form $A_2BB'O_6$ due to the $BO_6$ octahedral distortions induced by different radius of B and B′.[15] **Figure 1**A shows the typical cubic crystal structure of BFNO similar to $BaTiO_3$. $Ti^{4+}$ was replaced by $Nb^{5+}$ and $Fe^{3+}$ in the molar ratio of 1:1 to keep the charge in balance. The crystal structure has corner connected $FeO_6$ and $NbO_6$ octahedron and oxygen coordinated Ba cations, located in the octahedron. The perfect structure of octahedral connection results in a cubic lattice. On the other hand, the $FeO_6$ and $NbO_6$ octahedrons are arranged alternately in the crystal structure. As shown in Figure 1B, the crystal structure is refined by the Rietveld method with $R_p$ = 4.38% and $Rw_p$ = 5.85%. BFNO strictly crystallizes in a cubic system (space group Pm-3m), with lattice constants of a = b = c = 3.99234 Å, $\alpha = \beta = \gamma = 90°$, which matches previous report on the $PbFe_{0.5}Nb_{0.5}O_3$.[18] That confirms that the as-prepared BFNO is our designed perovskite with mixed Fe and Nb cations at B site. However, BFNO exhibit a perfect cubic phase with less distortion than our expectation. Figure 1C exhibits the UV–vis diffuse reflectance spectra (DRS) of $BaTiO_3$ and BFNO. It should be noted that there exists band tail adsorption in the UV–vis spectra of BFNO, which are related to the oxygen vacancy. According to the Rappe's explanation,[15] BNFO may contain trace amount $Fe^{2+}$, which results in oxygen vacancy in the lattice. Nb-containing ferroelectric perovskites have been shown to tolerate a high concentration of vacancies so B-site Nb ions should be able to accommodate the $Fe^{2+}$–oxygen vacancy combination. BFNO should contain oxygen vacancy and be noted as $Ba_2NbFeO_{6-x}$. $BaTiO_3$ is a typical perovskite, which exhibits UV light absorption less than 400 nm. While BFNO exhibits dark green color and strong visible light absorption in the visible light region up to 550 nm. The optical band gap of a semiconductor can be estimated from the Tauc plot, which is converted $(\alpha h\nu)^r$ versus $h\nu$ from the UV–vis spectrum, in which $\alpha$, $h$, and $\nu$ are the absorption coefficient, Planck constant, and light frequency, respectively. Where $r = 2$ for a direct allowed transitions, $r = 1/2$ for an indirect allowed transitions, $r = 2/3$ for direct forbidden transitions and $r = 1/3$ indirect forbidden transition, respectively. The Tauc plot (Figure S1A, Supporting Information) of BFNO, indicating that optical band gap of BFNO is about 2.29 eV. To elucidate the origin of the band gap of BFNO, we examined the electronic structure of BFNO with density functional theory. Density of state (DOS) calculation (Figure S2, Supporting Information) indicates that valance band maximum (VBM) is originated from the Ni 3d and O 2p state, and conduction band minimum (CBM) is mainly contributed from Fe 3d state. Nb 4d state provides a relatively

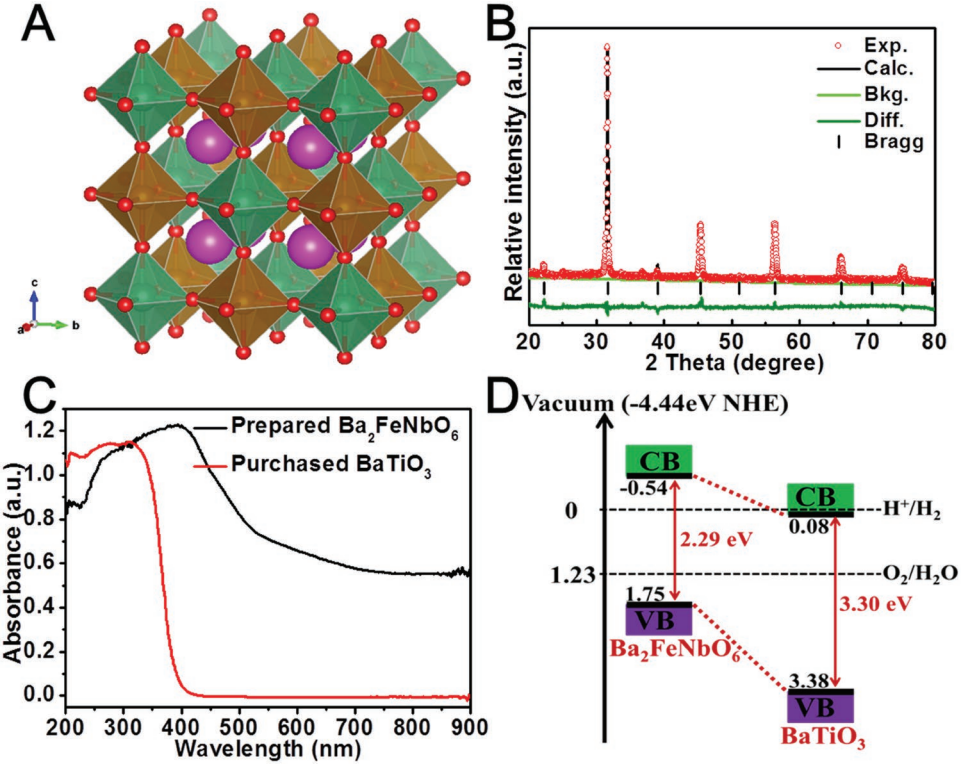


**Figure 1.** The crystal structure A) of $Ba_2FeNbO_6$ (BFNO; Ba, pink; Fe, tawny; Nb, green; O, red). B) The Rietveld refinement of X-ray diffraction pattern of as-prepared BFNO. Diffusion reflectance UV–vis spectra C) of $BaTiO_3$ and BFNO. D) Energy-level diagram based on UPS results showing the valence band and optical band gap ($E_g$) from Tauc plot of as-prepared BFNO and $BaTiO_3$.

weak contribution on the conduction band. The above results indicate that the narrow band gap mainly contribute from the incorporation of $Fe^{3+}$ at the B site. Furthermore, ultraviolet photoelectron spectroscopy (UPS) is employed to determine the valance band position of BFNO (Figure S1B, Supporting Information). Figure 1D illustrates the band structure of BFNO and $BaTiO_3$. The conduction band (CB) of $BaTiO_3$ is close to the standard potential of the normal hydrogen electrode (NHE). The valance band (VB) is far below the potential of water oxidation.[19] In the case of BFNO, VB calculated from the UPS is about 1.75 eV versus NHE. Combined with the optical band gap from Tauc plot, the VB and conduction band (CB) of BFNO straddle the water oxidation and reduction potentials. The possible reason is the electronegativity of Nb (1.60) and Fe (1.83) is larger than that of Ti (1.54). That will decrease the difference between metal at B site and O.

Although BFNO exhibits strong absorption in the visible light region and suitable band structure for water splitting, its photocatalytic performance for $H_2$ production is quite low (Figure S3, Supporting Information). We infer the reason might be the low charge separation efficiency like in the photovoltaic devices.[16] According to the previous report,[15] the solid solutions formed by BFNO with other perovskite may promote the charge separation process. Here, we further construct $SrTiO_3$-$Ba_2FeNbO_6$ (STO-BFNO) solid solutions instead of $BaTiO_3$-$Ba_2FeNbO_6$ solid solutions due to appropriate energy band structure of $SrTiO_3$ for photocatalytic water splitting. STO-BFNO solid solutions are synthesized through a simple one-step molten salts route in NaCl and KCl at 800 °C. The XRD patterns as shown in **Figure 2**A, the as-synthesized solid solutions exhibit a typical cubic phase as $SrTiO_3$ (JCPDS no. 35–0734). According to the Scherrer equation, the sizes of as-prepared nanoparticles are estimated to be 98.3, 80.7, 76.3, and 72.1 nm for $SrTiO_3$ and STO-BFNO-*n* (*n* = 0.25, 0.5, and 1.0), respectively, where the molar ratio of $SrTiO_3$ to BFNO is 10:*n*. The enlarged XRD patterns of above samples show the (110) diffraction peaks shift gradually (Figure 2B) from 32.42 to 32.35, 32.29, and 32.19 for $SrTiO_3$ and STO-BFNO-*n* (*n* = 0.25, 0.5, and 1.0), respectively. No BFNO diffraction peaks are observed in the solid solutions samples. Those results indicate that the as-prepared samples are not mixtures of $SrTiO_3$ and BFNO, but solid solution.

Transmission electron microscopy (TEM) images (**Figure 3**A,B and Figure S4 and S5, Supporting Information) disclose that the as-prepared STO-BFNO solid solutions are highly crystalline and the sizes are below 100 nm. The high resolution TEM (HR-TEM) images further display that the lattice fringe spacing is 0.278 nm for STO-BFNO-0.5, which locates between those of $SrTiO_3$ (0.276 nm) and BFNO (0.288 nm). Furthermore, EELS is used to establish the distribution of all elements in the solid solution. A bright field TEM and the corresponding EELS elements (Sr, Ti, O, Ba, Fe, and Nb) mapping images are displayed in Figure 3C. The uniform distribution of all elements over the whole area of solid solution suggests a homogeneous distribution of BFNO and without any phase separation. The above results suggest that STO-BFNO solid solutions are obtained via this simple molten salts route.

As a wide band gap perovskite oxide, $SrTiO_3$ presents a white powder, while the STO-BFNO solid solutions show light green and turn into darker with the increase of BFNO fraction (Figure S6, Supporting Information). The DRS UV–vis spectra are presented in **Figure 4**A. Compared with $SrTiO_3$, the band edge shifts toward visible light and absorption band at ≈450 nm is observed with the increase of BFNO fraction. This sub-gap absorption might be related to the defect in the STO-BFNO solid solution. When $Ti^{4+}$ ions are replaced by $Fe^{3+}$ (a few $Fe^{2+}$) and $Nb^{5+}$ ions, and $Sr^{2+}$ ions are replaced by $Ba^{2+}$. This substitution will generate the oxygen vacancy. The corresponding Tauc plot of these STO-BFNO solid solutions are shown in Figure 4B. It clearly shows that the optical band gap continuously decreases with the increase of BFNO in the solid solutions. The band gap ($E_g$) changes from 3.31 eV for $SrTiO_3$ to 3.08, 2.92, and 2.76 eV for STO-BFNO-*n* (*n* = 0.25, 0.5, and 1.0), respectively.

In order to determine the energy band structure of these solid solutions, UPS measurements are carried out and shown in Figure S5A–D of the Supporting Information. The valence band energy ($E_v$) of STO-BFNO solid solutions, which are calculated to be 6.70, 6.59, 6.53, and 6.48 eV (vs vacuum level) for $SrTiO_3$ and STO-BFNO-*n*, respectively, by subtracting the width of the He I UPS spectra from the excitation energy (21.22 eV).[20] According to the reference standard for which 0 V versus NHE equals to –4.44 eV versus $E_{vac}$ (vacuum level),[21] the $E_v$ are calculated to be 2.26 for $SrTiO_3$, and 2.15, 2.09, and

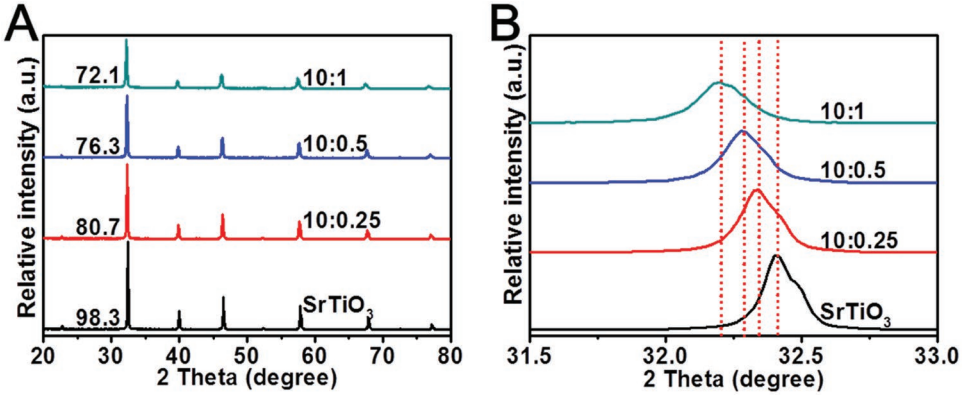


**Figure 2.** X-ray diffraction patterns of STO-BFNO solid solutions. A) Full scale, B) enlarge within 31.5°–33.0°.

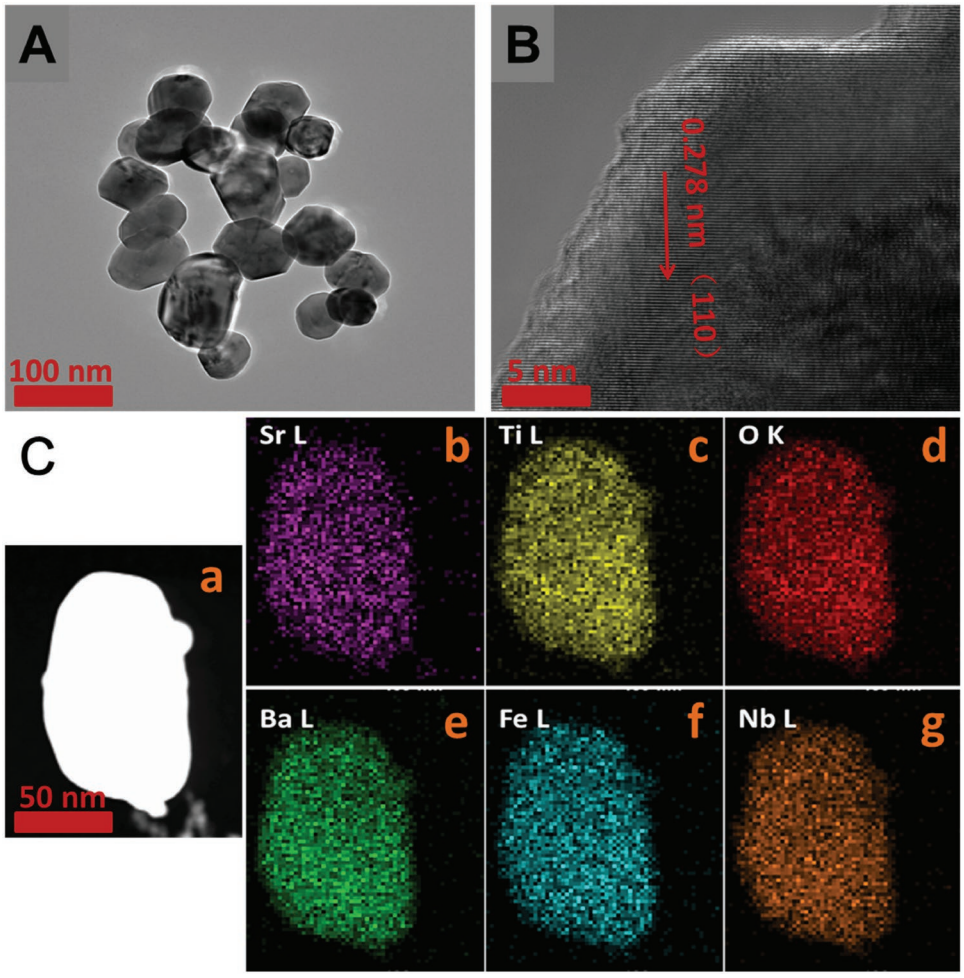


**Figure 3.** Transmission electron microscopy (TEM) images of STO-BFNO-0.5 A) low magnification TEM image, B) high resolution TEM image. C) EELS mapping images of STO-BFNO-0.5 (a) zero-energy loss bright field image, (b) Sr element mapping, (c) Ti element mapping, (d) O element mapping, (e) Ba element imaging, (f) Fe element mapping, and (g) Nb element mapping.

2.04 versus NHE for STO-BFNO-$n$ ($n$ = 0.25, 0.5, and 1.0), respectively. The VB position of solid solutions are keeping rise up in the energy level diagram, but it still lower than water oxidation potential. The CB of solid solutions can be calculated from the $E_v$ (energy level of VB) subtracted with $E_g$. The CB also show decreasing trend by increasing the amount of BFNO, while they locate above the potential of NHE in all cases. These results are listed in Table S1 of the Supporting Information

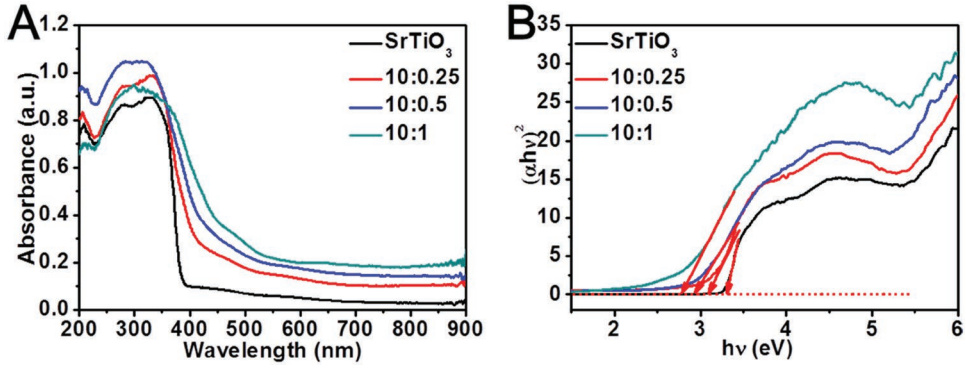


**Figure 4.** A) Diffusion reflection UV–vis spectra and B) the Tauc plot of transformed Kubelka–Munk function versus the energy of as-prepared STO-BFNO solid solutions.

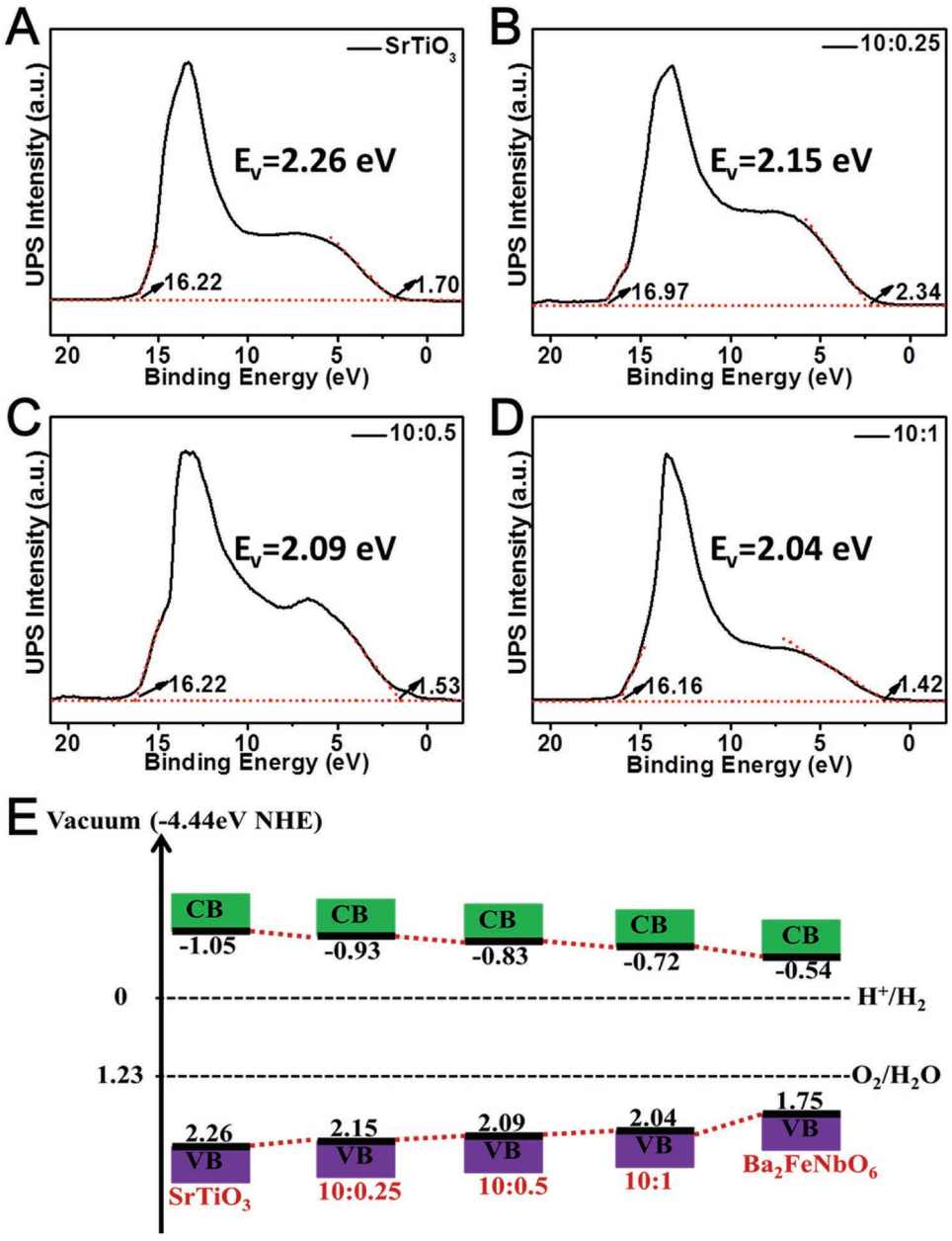


**Figure 5.** UV photoelectron spectroscopy spectra of A) $SrTiO_3$, B) STO-BFNO-0.25, C) STO-BFNO-0.5, and D) STO-BFNO-1. E) Energy level diagram of $SrTiO_3$, STO-BFNO solid solutions, and BFNO nanocrystals.

and **Figure 5**E. Usually, photocatalysts with higher specific surface areas are beneficial for the enhancement of photocatalytic performance. The Brunauer–Emmett–Teller (BET) surface area and pore size of the samples are characterized using $N_2$ adsorption–desorption isotherm shown in Figure S7 in the Supporting Information. It exhibits a type-III isotherm with a type-D hysteresis loop, indicating a macroporous structure.[22] The BET surface area are determined to be 4.27, 4.96, 5.09, 5.54, and 5.57 $m^2\ g^{-1}$ of STO-BFNO solid solutions (Figure S8, Supporting Information), which appears a slight increase because of the decrease of size with the increase of BFNO amount in the solid solutions.

**Figure 6**A,B shows the $H_2$ production of STO-BFNO solid solutions when loaded with 1.0 wt% Pt as cocatalyst under visible light ($\lambda > 420$ nm) irradiation. $SrTiO_3$ presents no photocatalytic $H_2$ production activity ($\lambda > 420$ nm). It exhibits obvious photocatalytic activity after forming solid solutions. The highest photocatalytic $H_2$ production rate is 7.15 μmol $h^{-1}$ for 50 mg STO-BFNO-0.5 sample under irradiation of visible light ($\lambda > 420$ nm). Figure 5C displays the wavelength dependence of $H_2$ production rate for STO-BFNO-0.5 solid solution. The active wavelength even reaches 500 nm. The corresponding apparent quantum efficiency (AQE) of 0.52% is obtained at 420 nm with a band-pass filter (420 ± 10 nm). The STO-BFNO photocatalysts

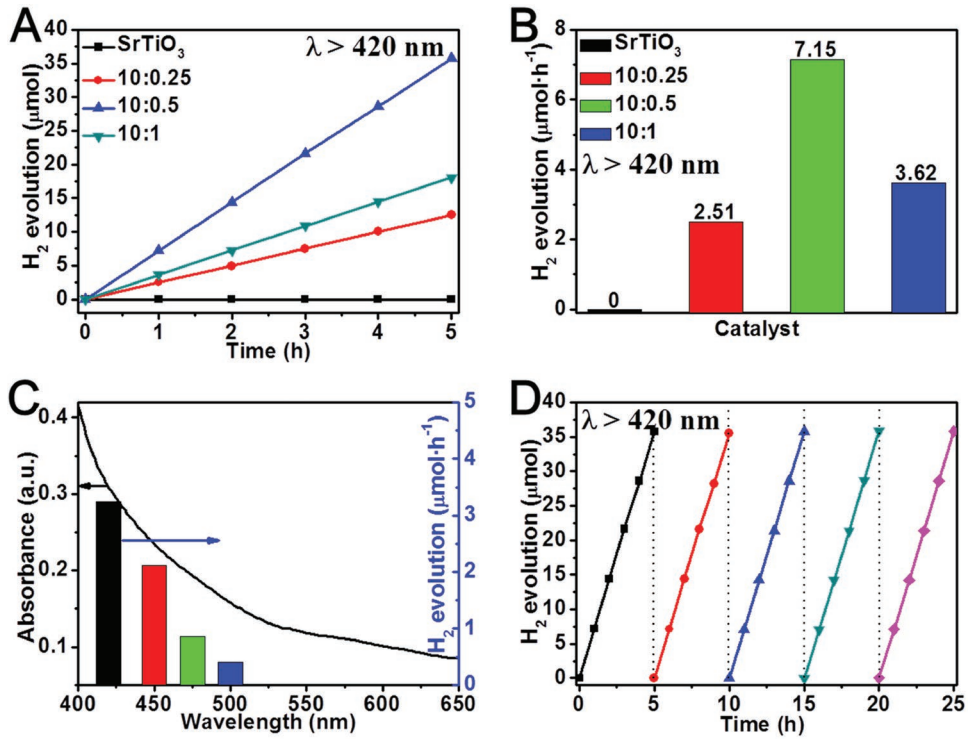


**Figure 6.** A) $H_2$ production and B) $H_2$ production rate of STO-BFNO solid solutions. The wavelength dependence of C) $H_2$ production rate and D) recycling measurements of $H_2$ production for STO-BFNO-0.5 solid solution.

also have an excellent stability according to the recycles measure of photocatalytic $H_2$ production (Figure 5D). After five recycles, none of recession of photocatalytic activity is observed.

The photoluminescent spectra and photocurrent test results are shown in Figure S9 of the Supporting Information. The PL peak intensity of STO-BFNO solid solutions reveals a significant decrease when the solid solutions are forming. It illustrates that these solid solutions samples have a relatively low radiative recombination and slow carrier mobility.[23] In Figure S9B of the Supporting Information, when the visible light ($\lambda > 420$ nm) is successively shuttled on and off, a series of photocurrent signals can be detected. $SrTiO_3$ presents a negligible photocurrent. It exhibits obvious photocurrent signals when forming solid solutions. The maximal photocurrent is observed of STO-BFNO-0.5 solid solution. Those photocurrent results are consistent with the photocatalytic activity measurements. These results indicate that the photogenerated charges could separate in the solid solutions. Further raising the charge separation efficiency of solid solutions could improve the photocatalytic performance for these perovskite oxides with narrow band gap. This will open a new avenue for the construction of visible light photocatalysts.

In summary, we develop a simple one-step molten salts route to fabricate narrow band gap perovskite $Ba_2FeNbO_6$ with substitutional B site. Although it shows a narrow band gap of ≈2.29 eV and suitable band energy level for water splitting, its photocatalytic performance is quite poor due to low charge separation efficiency. Furthermore, a series of STO-BFNO ($SrTiO_3$-$Ba_2FeNbO_6$) solid solutions are synthesized through similar route. XRD, TEM images, and EEEL elemental mapping indicate the STO-BFNO solid solutions are uniformly formed. The color can be turned from white to yellow green. The optimal molar ratio of STO to BFNO is about 10:0.5 and the $H_2$ production rate of corresponding STO-BFNO-0.5 is 7.15 μmol $h^{-1}$ for 50 mg samples under visible light irradiation.

## Experimental Section

*Chemicals and Materials*: $SrCO_3$ (AR, 99.8%), $BaCO_3$ (AR, 99%), $BaTO_3$ (AR, 99.9%), $Nb_2O_5$ (AR, 99.9%), and $Fe_2O_3$ (30 nm, 99.5%) are purchased from Aladdin Reagent Company. Methanol (AR, 99.5%), NaCl (AR, 99.8%), and KCl (AR, 99.8%) are purchased from Sinopharm Chemical Reagent Company. P25 $TiO_2$ is purchased from Degussa AG, Germany. All chemicals are used without any further purification.

*Synthesis of $Ba_2FeNbO_6$ Nanocrystals*: NaCl and KCl serves as molten salts medium because of their low melting temperature (670 °C). In the typical synthesis of $Ba_2FeNbO_6$ nanocrystals, $BaCO_3$, $Nb_2O_5$, $Fe_2O_3$, NaCl, and KCl are mixed in an overall stoichiometric ratio of 1:0.5:0.5:50: 50. The mixtures are put into an alumina crucible and then heated to 800 °C at a heating rate of 5 °C $min^{-1}$ in a muffle furnace and maintained at this temperature for 5 h. After cooling down to room temperature, the samples are washed with deionized distilled water several times to remove remaining salts impurity and dried in an oven at 60 °C for 12 h.

*Synthesis of $SrTiO_3$ Nanocrystals*: In the typical synthesis of $SrTiO_3$ nanocrystals, $SrCO_3$, $TiO_2$, NaCl, and KCl are mixed in an overall stoichiometric ratio of 1:1:50:50, other synthetic conditions are same as the synthesis of $Ba_2FeNbO_6$ nanocrystals.

*Synthesis of $SrTiO_3$-$Ba_2FeNbO_6$ Solid Solutions Nanocrystals*: In the typical synthesis of $SrTiO_3$-$Ba_2FeNbO_6$ solid solutions nanocrystals, $SrCO_3$, $TiO_2$, $BaCO_3$, $Nb_2O_5$, $Fe_2O_3$, NaCl, and KCl are mixed in an

overall stoichiometric ratio of 1:1:*x*:0.25*x*:0.25*x*:50:50 ($x$ = 0.05, 0.1, and 0.2), other synthetic conditions are same as the synthesis of $Ba_2FeNbO_6$ nanocrystals.

*Characterizations*: TEM images are taken using an FEI Tecnai G2 operated at 200 kV. UPS measurements are performed with an unfiltered He I (21.22 eV) gas discharge lamp and a total instrumental energy resolution of 100 meV. The crystalline structure is recorded by using an XRD (Bruker AXS D8 Focus), using Cu K$\alpha$ radiation ($\lambda$ = 1.54056 A). BET specific surface area is measured using a Micromeritics Gemini V Surface Area and Pore Size Analyzer. The UV–vis absorption spectra are recorded on an UV-3600 UV–vis-NIR scanning spectrophotometer (Shimadzu).

*Photocatalytic Activity Measurements*: The 50 mg of STO-BFNO ($SrTiO_3$-$Ba_2FeNbO_6$) solid solutions photocatalysts loaded with 1.0 wt% Pt is placed into an aqueous methanol solution (120 mL, 25 vol%) in a closed gas circulation system (Perfect Light Company Labsolar-III (AG)). The visible light and band-pass irradiations are obtained from a 300 W Xe lamp (PLS-SXE 300, Beijing Trusttech Co. Ltd, China) with a UVCUT-420 nm filter (Newport) and band-pass filters (centered at 420, 450, 475, and 500 nm). The evolved gases are detected in situ by using an online gas chromatograph (GC-2014C, Shimadzu) equipped with a thermal conductivity detector (TCD). The average intensity of irradiation is determined by an FZ-A spectroradiometer (Photoelectric Instrument Factory of Beijing Normal University). The quantum efficiency is calculated from equation

$$QE = \frac{2 \times \text{the number of evolved } H_2 \text{ molecules}}{\text{the number of incident photons}} \times 100\% \quad (1)$$

## Supporting Information

Supporting Information is available from the Wiley Online Library or from the author.

## Acknowledgements

The authors thank the National Natural Science Foundation of China (Nos. 21301166, 21201159, and 61361166004), Supported by open research fund program of State Key Laboratory of Luminescence and Applications (CIOMP, CAS). Z.S. thanks financial support from Beijing High-level Talent program. D.Z. thanks the Guangdong Natural Science Foundation (2016A030313081).

Received: May 4, 2016
Revised: July 10, 2016
Published online: September 22, 2016

[1] X. Li, J. Wen, J. Low, Y. Fang, J. Yu, *Sci. China Mater.* **2014**, *57*, 70.
[2] X. Chen, S. Shen, L. Guo, S. S. Mao, *Chem. Rev.* **2010**, *110*, 6503.
[3] a) H. Yan, J. Yang, G. Ma, G. Wu, X. Zong, Z. Lei, J. Shi, C. Li, *J. Catal.* **2009**, *266*, 165; b) D. Jing, L. Guo, *J. Phys. Chem. B* **2006**, *110*, 11139; c) R. Costi, A. E. Saunders, E. Elmalem, A. Salant, U. Banin, *Nano Lett.* **2008**, *8*, 637; d) W.-T. Yao, S.-H. Yu, S.-J. Liu, J.-P. Chen, X.-M. Liu, F.-Q. Li, *J. Phys. Chem. B* **2006**, *110*, 11704.
[4] a) A. Kleiman-Shwarsctein, Y.-S. Hu, A. J. Forman, G. D. Stucky, E. W. McFarland, *J. Phys. Chem. C* **2008**, *112*, 15900; b) J. Luo, P. A. Maggard, *Adv. Mater.* **2006**, *18*, 514; c) C. Kormann, D. W. Bahnemann, M. R. Hoffmann, *J. Photochem. Photobiol., A* **1989**, *48*, 161; d) A. Tanaka, K. Hashimoto, H. Kominami, *J. Am. Chem. Soc.* **2014**, *136*, 586; e) F. Wang, C. Di Valentin, G. Pacchioni, *ChemCatChem* **2012**, *4*, 476.
[5] Z. Zou, J. Ye, K. Sayama, H. Arakawa, *Nature* **2001**, *414*, 625.
[6] H. Yamashita, M. Harada, J. Misaka, M. Takeuchi, K. Ikeue, M. Anpo, *J. Photochem. Photobiol., A* **2002**, *148*, 257.
[7] R. Asahi, T. Morikawa, T. Ohwaki, K. Aoki, Y. Taga, *Science* **2001**, *293*, 269.
[8] a) J. H. Park, S. Kim, A. J. Bard, *Nano Lett.* **2006**, *6*, 24; b) H. Irie, Y. Watanabe, K. Hashimoto, *Chem. Lett.* **2003**, *32*, 772.
[9] a) R. Abe, M. Higashi, K. Domen, *J. Am. Chem. Soc.* **2010**, *132*, 11828; b) M. Higashi, K. Domen, R. Abe, *J. Am. Chem. Soc.* **2013**, *135*, 10238; c) K. Maeda, M. Higashi, B. Siritanaratkul, R. Abe, K. Domen, *J. Am. Chem. Soc.* **2011**, *133*, 12334; d) T. Minegishi, N. Nishimura, J. Kubota, K. Domen, *Chem. Sci.* **2013**, *4*, 1120; e) C. Pan, T. Takata, M. Nakabayashi, T. Matsumoto, N. Shibata, Y. Ikuhara, K. Domen, *Angew. Chem. Int. Ed.* **2015**, *54*, 2955.
[10] J. Xu, C. Pan, T. Takata, K. Domen, *Chem. Commun.* **2015**, *51*, 7191.
[11] A. Bhalla, R. Guo, R. Roy, *Mater. Res. Innovations* **2000**, *4*, 3.
[12] a) Q. Jia, A. Iwase, A. Kudo, *Chem. Sci.* **2014**, *5*, 1513; b) J. Shi, L. Guo, *Prog. Nat. Sci.: Mater. Int.* **2012**, *22*, 592.
[13] W. Zhang, J. Tang, J. Ye, *Chem. Phys. Lett.* **2006**, *418*, 174.
[14] a) J. W. Bennett, I. Grinberg, A. M. Rappe, *J. Am. Chem. Soc.* **2008**, *130*, 17409; b) G. Gou, J. W. Bennett, H. Takenaka, A. M. Rappe, *Phys. Rev. B* **2011**, *83*, 205115; c) T. Qi, I. Grinberg, A. M. Rappe, *Phys. Rev. B* **2011**, *83*, 224108; d) H. W. Eng, P. W. Barnes, B. M. Auer, P. M. Woodward, *J. Solid State Chem.* **2003**, *175*, 94; e) A. Y. Borisevich, H. J. Chang, M. Huijben, M. P. Oxley, S. Okamoto, M. K. Niranjan, J. Burton, E. Tsymbal, Y.-H. Chu, P. Yu, *Phys. Rev. Lett.* **2010**, *105*, 087204; f) F. Wang, I. Grinberg, A. M. Rappe, *Appl. Phys. Lett.* **2014**, *104*, 152903.
[15] I. Grinberg, D. V. West, M. Torres, G. Gou, D. M. Stein, L. Wu, G. Chen, E. M. Gallo, A. R. Akbashev, P. K. Davies, J. E. Spanier, A. M. Rappe, *Nature* **2013**, *503*, 509.
[16] R. Nechache, C. Harnagea, S. Li, L. Cardenas, W. Huang, J. Chakrabartty, F. Rosei, *Nat. Photonics* **2015**, *9*, 61.
[17] H. Liu, J. Chen, Y. Ren, L. Zhang, Z. Pan, L. Fan, X. Xing, *Adv. Electron. Mater.* **2015**, *1*, 1400051.
[18] L. Nathascia, S. Philippe, L. Alessandra Geddo, *J. Phys. Condens. Matter* **1999**, *11*, 3489.
[19] Y. Xu, M. A. Schoonen, *Am. Mineral.* **2000**, *85*, 543.
[20] a) J. Liu, Y. Liu, N. Liu, Y. Han, X. Zhang, H. Huang, Y. Lifshitz, S.-T. Lee, J. Zhong, Z. Kang, *Science* **2015**, *347*, 970; b) W.-J. Chun, A. Ishikawa, H. Fujisawa, T. Takata, J. N. Kondo, M. Hara, M. Kawai, Y. Matsumoto, K. Domen, *J. Phys. Chem. B* **2003**, *107*, 1798.
[21] a) Y. Matsumoto, *J. Solid State Chem.* **1996**, *126*, 227; b) C. G. Van de Walle, J. Neugebauer, *Nature* **2003**, *423*, 626.
[22] a) D. Liu, Y. Yao, D. Tang, S. Tang, Y. Che, W. Huang, *Int. J. Coal Geol.* **2009**, *79*, 97; b) M. Khalfaoui, S. Knani, M. Hachicha, A. B. Lamine, *J. Colloid Interface Sci.* **2003**, *263*, 350; c) J. Wang, X. Yang, D. Wu, R. Fu, M. S. Dresselhaus, G. Dresselhaus, *J. Power Sources* **2008**, *185*, 589.
[23] a) P. Blom, M. Vissenberg, J. Huiberts, H. Martens, H. Schoo, *Appl. Phys. Lett.* **2000**, *77*, 2057; b) A. Babel, S. A. Jenekhe, *Macromolecules* **2003**, *36*, 7759; c) T. M. Burke, M. D. McGehee, *Adv. Mater.* **2014**, *26*, 1923; d) Z. Fan, P.-C. Chang, J. G. Lu, E. C. Walter, R. M. Penner, C.-H. Lin, H. P. Lee, *Appl. Phys. Lett.* **2004**, *85*, 6128.

  